

Article

A Novel Multi-Dimensional Composition Method Based on Time Series Similarity for Array Pulse Wave Signals Detecting

Hongjie Zou ^{1,2,3}, Yitao Zhang ^{1,3,*}, Jun Zhang ^{1,2,3}, Chuanglu Chen ^{1,2,3}, Xingguang Geng ^{1,2,3}, Shaolong Zhang ^{1,2,3} and Haiying Zhang ^{1,2,3}

¹ Institute of Microelectronics of Chinese Academy of Sciences, Beijing 100029, China; zouhongjie@ime.ac.cn (H.Z.); zhangjun@ime.ac.cn (J.Z.); chenchuanglu@ime.ac.cn (C.C.); gengxingguang@ime.ac.cn (X.G.); zhangshaolong@ime.ac.cn (S.Z.); zhanghaiying@ime.ac.cn (H.Z.)

² University of Chinese Academy of Sciences, Beijing 100049, China

³ Beijing Key Laboratory for Next Generation RF Communication Chip Technology, Beijing 100029, China

* Correspondence: zhangyitao@ime.ac.cn

Received: 30 September 2020; Accepted: 9 November 2020; Published: 14 November 2020



Abstract: Pulse wave signal sensed over the radial artery on the wrist is a crucial physiological indicator in disease diagnosis. The sensor array composed of multiple sensors has the ability to collect abundant pulse wave information. As a result, it has gradually attracted the attention of practitioners. However, few practical methods are used to obtain a one-dimensional pulse wave from the sensor array's spatial multi-dimensional signals. The current algorithm using pulse wave with the highest amplitude value as the significant data suffers from low consistency because the signal acquired each time differs significantly due to the sensor's relative position shift to the test area. This paper proposes a processing method based on time series similarity, which can take full advantage of sensor arrays' spatial multi-dimensional characteristics and effectively avoid the above factors' influence. A pulse wave acquisition system (PWAS) containing a micro-electro-mechanical system (MEMS) sensor array is continuously extruded using a stable dynamic pressure input source to simulate the pulse wave acquisition process. Experiments are conducted at multiple test locations with multiple data acquisitions to evaluate the performance of the algorithm. The experimental results show that the newly proposed processing method using time series similarity as the criterion has better consistency and stability.

Keywords: micro-electro-mechanical system (MEMS); flexible sensor array; time series similarity; Dynamic Time Warping (DTW); pulse signal

1. Introduction

Like the electrocardiography (ECG) signal, the heart's regular contraction and diastole produce a pulse wave signal [1]. The pulse signal conducted by the blood flowing through the human body's various organs contains a wealth of physiological and pathological information [2,3]. The diagnosis of diseases through pulse signals has not only been highly approved by traditional Chinese medicine (TCM) but has also received increasing attention from modern medicine [4–6]. In TCM diagnosis, the pulse wave collection position is mainly distributed in the radial artery area near the subject's wrist. As plotted in Figure 1a, along the direction from the palm to the arm, it is divided into three positions: Cun, Guan, and Chi [7,8]. Usually, the pulse waveform is also related to the static force applied to the test area, divided into three segments: Fu, Zhong, and Chen, according to the course of the force from light to heavy, as shown in Figure 1b [8].

However, this diagnostic method that relies on long-term training and rich experience has specific subjective errors. Therefore, a digital acquisition system capable of objectively measuring pulse wave signals has been proposed and studied. Various types of sensors, including piezoelectric [9–11], piezoresistive [12–14], photoelectric [15–17], and ultrasonic [18,19] sensors, have been developed and improved to capture weak pulse wave signals. With advances in sensors, manufacturing technology, and signal processing methods, a wide variety of pulse wave acquisition systems have emerged [20–24]. The equipment used to assist TCM diagnosis has expanded from a single-probe type [25] to a three-probe type [22,26] that can collect three positions of Cun, Guan, and Chi at the same time, and even reaches a five-probe type [21]. The signal acquisition for a single test location is also updated from a single sensor to a sensor array composed of multiple sensors [24,27].

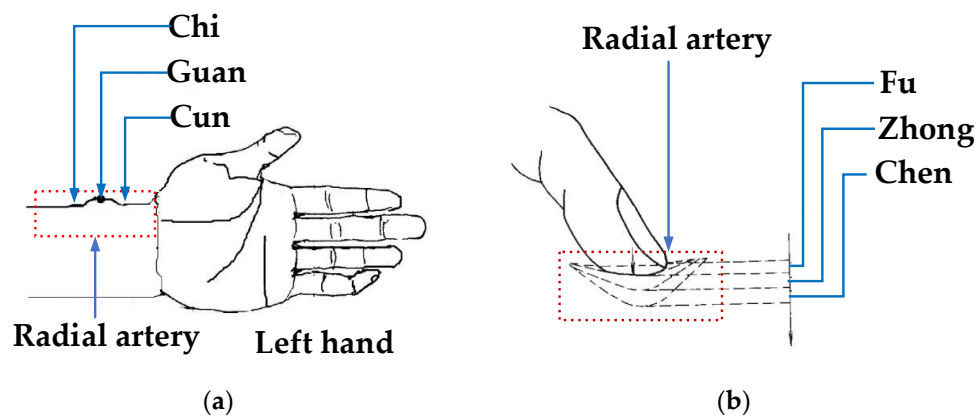


Figure 1. (a) Schematic diagram of the test locations of Cun, Guan, and Chi; (b) Diagram of different static pressure tests.

By comparing and analyzing the difference between the pulse wave waveform collected by a single sensor and the standard pulse waveform, it can assist the doctor in the diagnosis. However, it is impossible to obtain spatially relevant information, such as the pulse wave's length and width [8,25]. The acquisition system, including a sensor array, can acquire multi-dimensional pulse wave signals in space and then calculate the pulse wave's length and width characteristics to compensate for the defects, as mentioned above [23,24,27].

However, there are few studies on how to obtain a single valid and stable pulse waveform from multiple sensors [28,29]. Some researchers take the sensor with the highest amplitude value of the collected signal in a single cycle as the representative sensor. Moreover, the signal collected by this sensor is the effective pulse waveform of the whole sensor array [30]. Other researchers interpolate the spatial multi-dimensional signals collected by the sensor array to obtain a 3D pulse waveform signal map. The highest point in each three-dimensional pulse wave signal graph in one acquisition cycle is extracted as the pulse wave signal of the entire cycle [24,27]. The dynamic force applied to different sensors changes during multiple acquisitions due to slight differences in the test positions covered by the sensor arrays. This results in an unbalanced shift in pulse wave amplitude between sensors, with some sensors increasing and some decreasing pulse wave amplitude. The relative variation in signal amplitude makes it meaningless to select the representative sensor with the greatest amplitude or the effective pulse wave reference point.

This paper proposes a pulse wave processing method with waveform similarity as a criterion to solve the above problem. First, the pulse wave is examined to select valid waveforms that remove the effects of abnormal signals. Second, the similarity between the valid pulse wave signals is calculated and ranked. Meanwhile, the average power of the effective pulse wave signals in a single acquisition cycle is calculated and ranked. Then, based on the ranking results, the valid signals are linearly adjusted. Finally, all the adjusted valid signals are linearly superimposed to complete the entire algorithm. To verify the algorithm's performance, an experimental scheme consisting of a pulse wave

acquisition system (PWAS) and a single-point vibration system is designed. The former contains an array of micro-electro-mechanical system (MEMS) sensors that can be used to acquire spatially multi-dimensional signals. The latter acts as an input source for a stable pulse wave pressure. Experimental results show that the new algorithm can well eliminate the effect of the relative position shift of the test area and sensor arrays to obtain a stable and valid pulse waveform.

2. Materials and Methods

2.1. Pulse Wave Acquisition System

Figure 2a shows a PWAS consists of a sensor array module, a circuit module, and a program module with a graphical user interface (GUI) [27]. The acquisition module converts the pulse signal into a voltage signal, amplified and separated into a static force signal and a dynamic force signal by the circuit module, and finally processed by the program module and displayed on the terminal screen.

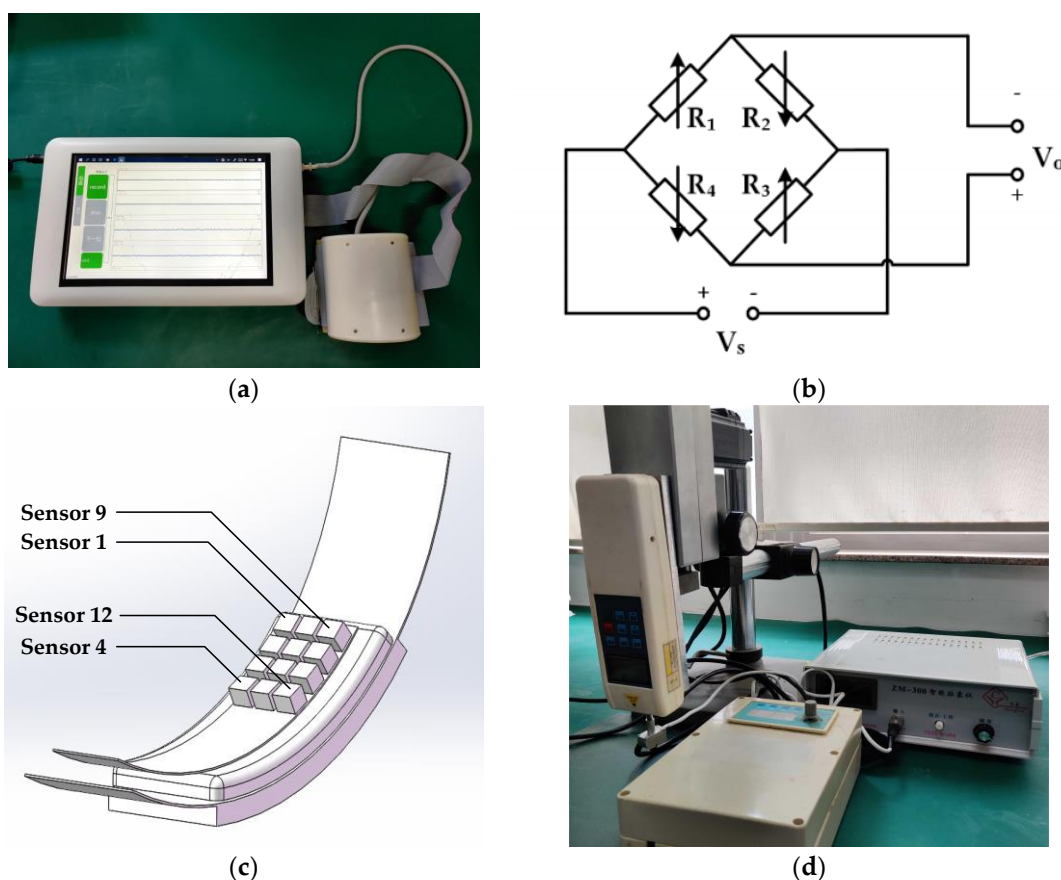


Figure 2. Acquisition devices for array sensor signals and single sensor signals. (a) Photograph of the pulse wave acquisition system (PWAS); (b) schematic diagram of the circuit structure of the sensor; (c) schematic diagram of the micro-electro-mechanical system (MEMS) sensor array; (d) photograph of the single-point pressure vibration generator (SPVG).

The MEMS pressure sensor array, rigid plastic housing, and inflatable cuff comprise the sensor array module. A MEMS pressure sensor chip (MPS20N0100D, MEMStek Co., Ltd.) was chosen as the critical component to form the sensor array [27], as shown in Figure 2b. The maximum pressure it can measure is 100 Kpa, which is more extensive than the range of static force variations. Non-linearity of 0.3% Full-scale (FS) and maximum stability of 0.2% Full-scale per year (FS/Y) guarantee the linearity, consistency, and stability of the sensor chip. The sensor's size is 5.5 mm × 3.6 mm × 4.5 mm, which makes it possible to form high-density sensor arrays. The MEMS pressure sensor array consists of 12 MEMS

sensors, divided into 4 rows and 3 columns, covering a test area of 18.6 mm × 20.3 mm. The housing is curved to ensure adequate contact between the acquisition module and human skin and to ease the testers' discomfort during the acquisition process. Cuff with polyurethane foam to distribute pressure evenly across the contact surface of the wrist and acquisition module. The inflated cuff can deliver a stepped pressure of 10 to 210 mmHg. The cuff pressure exerted on the wrist of the subject gradually increases in steps of 10 mmHg, each time stopping for a few seconds to collect both static and dynamic force signals of the pulse wave. After completing the entire acquisition process, the cuff undergoes a deflation process. The sampling frequency of the system is 218 Hz. Acquisition time is 15 s for each set static force. For the convenience of expression, each sensor in the sensor array is named sensor 1, sensor 2, sensor 3, . . . , sensor 12, in order of location, as shown in Figure 2c.

2.2. Single-Point Vibration Source Generator

This paper designed a single-point pressure vibration generator (SPVG) to investigate the effectiveness and stability of different pulse wave processing algorithms during multiple tests. As shown in Figure 2d, the SPVG consists of a vibration generator, a metal linkage, and a commercial pulse measurement device. The vibration generator is driven by a motor and can be set by the frequency generator to provide a vertical back and forth motion. The rigid metal connecting rod connects the vibration generator and the signal acquisition system, acting as an intermediary for transmitting vibration energy. Intelligent pulse meter ZM-300 [31,32], which conforms to the Chinese medical pulse detector's technical standard, is used to collect static force signals and dynamic force signals in real-time. The ZM-300 includes a 3 mm × 4 mm probe, a pulse wave output interface, and a pulse wave display interface. The probe consists of a single MEMS sensor that can measure static pressure from 0–250 g and dynamic pressure from 0–50 g.

2.3. Spatial Multi-Dimensional Pulse Wave Signal Processing Method

The processing of a spatial multi-dimensional pulse wave signal is divided into two main modules, as shown in Figure 3a. The first module focuses on removing noise and interference from the 12 dynamic pulse wave signals collected by PAWS using two sets of filters. The other module extracts the one-dimensional pulse wave signal from the filtered array signal using various pulse wave processing algorithms, as described in Figure 3b,d,e.

Pulse wave noise and interference consist of three main components: random noise, baseline drift, and 50 Hz power line interference. Random noise, distributed over the entire frequency range, is also present in the frequency band where pulse waves occur. Therefore, it is difficult to eliminate the noise using frequency-based filtering. The Sym8 wavelet function is chosen as the wavelet base to decompose the original signal into four layers. Hard threshold filtering is applied to each layer to reduce the random noise energy effectively. During the test results, the baseline drifts partly from the slow release of the sensor's additional pressure during cuff pressurization and partly from the testers' breathing. The former is below 0.1 Hz, while the latter is distributed in the range of 0.2 to 0.4 Hz. A zero-phase shift bandpass filter with a bandwidth of 0.5 Hz to 40 Hz can remove baseline drift and 50 Hz-frequency interference and avoid the relative shift of signal phase during filter processing. The following part is a detailed description of Algorithm I, Algorithm II, and Algorithm III.

Algorithm I The processing flow of Algorithm I is shown in Figure 3b, where x_1, x_2, \dots, x_{12} is the dynamic force pulse wave signal collected by 12 sensors. Max is the maximum value filter function, and its output is the maximum value of the input signal and the index where the maximum amplitude is. In an acquisition cycle, $x_{i,j}$ is the pulse wave signal value of the i -th sensor at the j -th sample point, $i \in M$, $j \in N$, where M is the number of sensors, and N is the number of sample points. The sample point r_i with the highest value of pulse wave amplitude is selected as a representative value of the i -th sensor by comparing the values of N sample points on the i -th sensor. Each sensor has a representative point, so M sensors have a total of M representative points. Comparing the above representative points, the aim is to find the maximum value and the index of the sensor where the maximum value is located. The former is

MAX the latter is m , as in Equation (1). The pulse wave signal collected by the m -th sensor during the current acquisition cycle is used as the pulse waveform graph as shown in Equation (2).

$$MAX = \max_{i \in M} \{r_i\} = \max_{i \in M} \{ \max_{j \in N} (x_{i,j}) \} \tag{1}$$

$$y = x_m \tag{2}$$

Algorithm II Before Algorithm II processing, the M -channel pulse wave signal needs to be reconstructed according to the spatial location of the acquisition sensor to facilitate interpolation fitting. As shown in Figure 3c, the spatial coordinates of sensor 1 are (1,1); along the positive X-axis, the spatial coordinates of sensor 4 are (4,1); and along the positive Y-axis, the spatial coordinates of sensor 9 are (1,3). There is a total of $M \times N$ sampling points in an acquisition cycle, where M is the number of sensors, and N is the number of sampling points of a single sensor in the cycle.

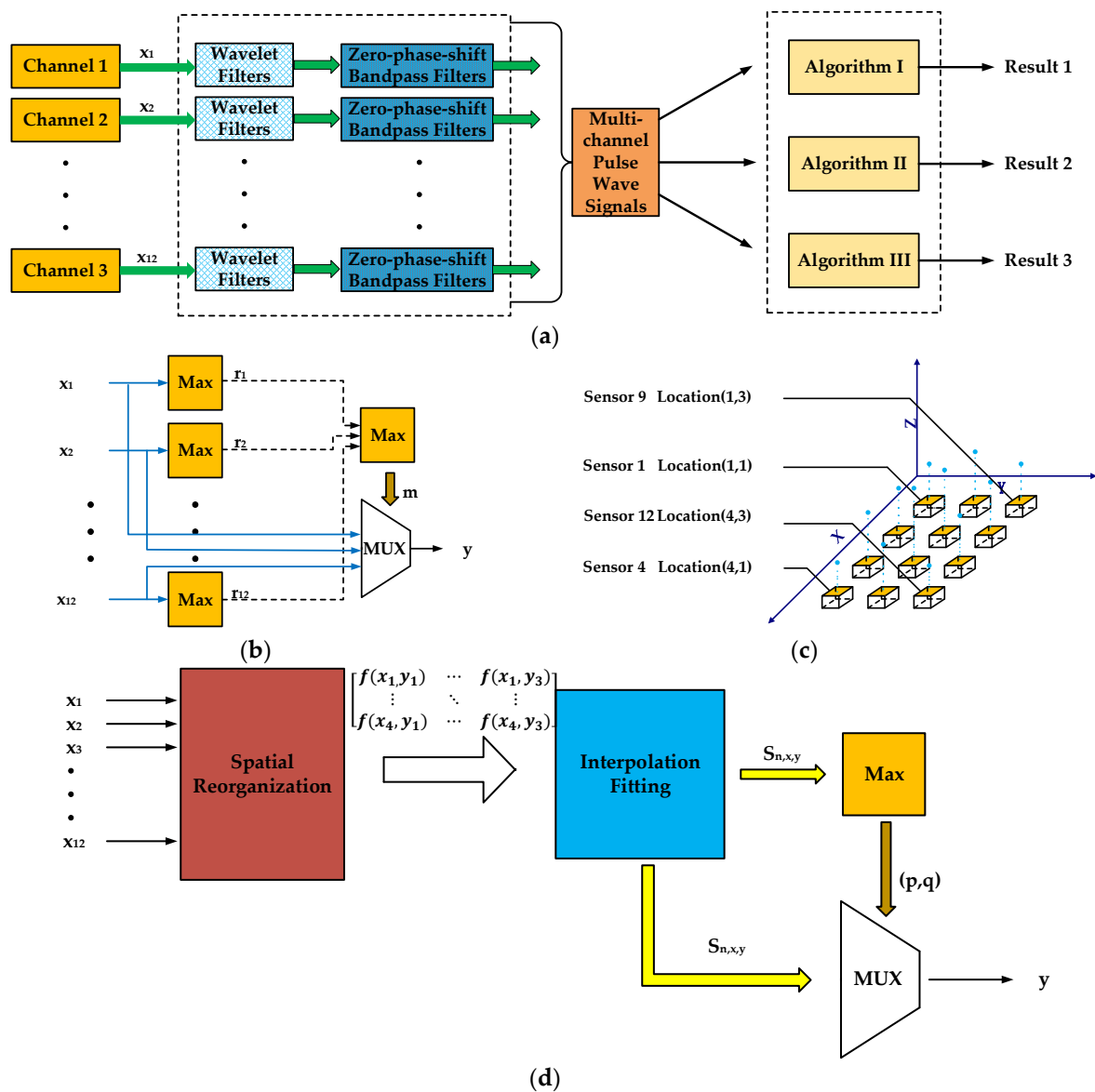


Figure 3. Cont.

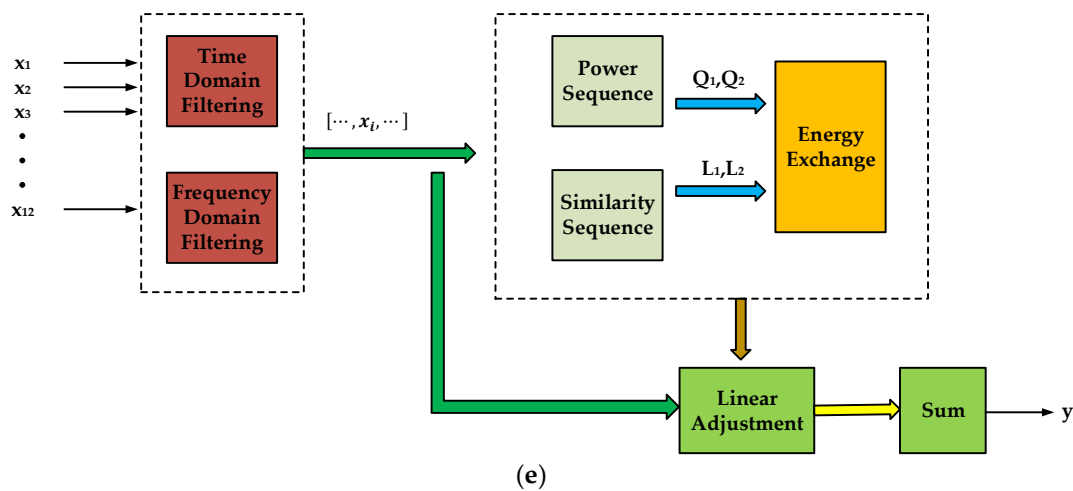


Figure 3. (a) Schematic diagram of the pulse wave signal processing flow; (b) block diagram of the Algorithm I process; (c) schematic diagram of spatial reconstruction of arrayed pulse wave signals; (d) block diagram of the Algorithm II process; (e) block diagram of the Algorithm III process.

$$f(x, y) = \sum_{i=0}^3 \sum_{j=0}^3 f(x_i, y_j)W(x - x_i)W(y - y_j) \tag{3}$$

$$W(x) = \begin{cases} (a + 2)|x|^3 - (a + 3)|x|^2 + 1 & |x| \leq 1 \\ a|x|^3 - 5a|x|^2 + 8a|x| - 4a & 1 < |x| < 2 \\ 0 & otherwise \end{cases} \tag{4}$$

$$MAX = s_{p,q} = \max_{n \in N} \{ \max_{x \in E, y \in F} S_{n,x,y} \} \tag{5}$$

$$y = S_{p,q} \tag{6}$$

The Bicubic Interpolation Algorithm [33] is implemented using a convolutional operation as in Equation (3) to compute the point $f(x, y)$ to be interpolated, where $f(x_i, y_j)$ is the 16 neighborhood points in the vicinity of $f(x, y)$. $W(x)$ in Equation (4) implements the convolutional kernel in Equation (3), and a is typically -0.5 . For each acquisition moment, E points are interpolated in the x -direction and F points are interpolated in the y -direction, producing a total number of $E \times F$ interpolation points, which are then fitted to the 3D pulse wave signal $S_{x,y}$. x and y are the horizontal and vertical coordinates of the interpolation point $S_{x,y}$, with $x \in E$ and $y \in F$, respectively. N samples can be interpolated to get N 3D pulse waveforms $S_{n,x,y}$, $n \in N$. Like Algorithm I, the points s with the highest amplitude value in each pulse waveform graph is used as the representative point. Therefore, there are a total of N representative points. As shown in Equation (5), the spatial coordinates (p, q) of the maximum value and the corresponding maximum value are recorded by comparing the values of N representative points sequentially. In one acquisition cycle, the one-dimensional pulse wave signal $S_{p,q}$ of the sensor array is formed by N points with coordinates (p, q) in the pulse waveform $S_{n,x,y}$, as in Equation (6).

Algorithm III The information carried by a single sensor pulse wave is limited and is susceptible to the influence of the sensor array’s position relative to the radial artery test area. Linear synthesis of multiple sensors can reduce the influence of a single sensor and increase the pulse wave acquisition system’s gain.

However, due to the area covered by the sensor array, which exceeds the test area, some of the sensors can only collect ambient noise and interference. Suppose the data from sensors are added to the data set. In that case, the pulse’s characteristics will be affected, and the reliability of the diagnosis will be reduced. Therefore, it is necessary to identify the effective pulse waveform before synthesizing the signal. Valid and invalid signals have many different characteristics in the time domain, as shown in

Figure 4a,c. The former has periodic peaks and troughs, and the time interval between adjacent peaks is within a specific range. Considering the human heart rate range of 55–160 beats/min, the lower limit of the time interval between adjacent peaks is 0.38 s and the upper limit is 1.09 s [34]. As shown in Figure 4b,d, the valid pulse wave signal’s spectral distribution is quite different from the invalid signal is. The spectral energy of the invalid signal is concentrated near 0 Hz. The energy of the effective signal is distributed in the range of 0.5 Hz to 25 Hz and is concentrated at a few specific frequency points. The signals are examined in the time and frequency domains, respectively, as in Equations (7) and (8). where T is the time interval between adjacent wave peaks, f is the frequency, and max is the frequency value at which the spectral energy is maximum. Only pulse wave signals that satisfy both conditions are valid.

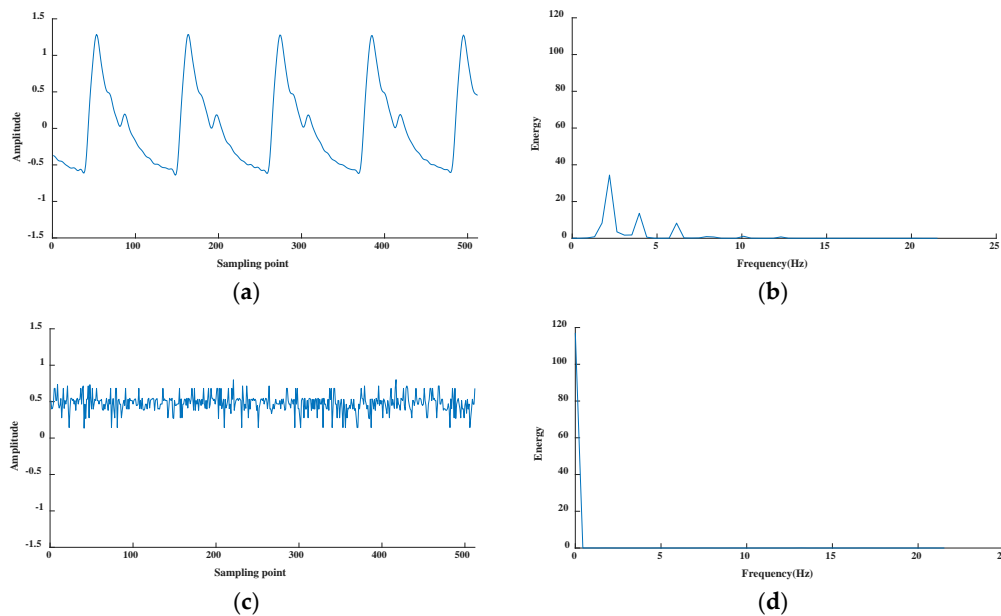


Figure 4. Signals and their spectra: (a) time domain diagram of valid pulse wave signal; (b) frequency domain diagram of valid pulse wave signal; (c) time domain diagram of noise signal; (d) frequency domain diagram of noise signal.

$$0.38 \text{ s} \leq T \leq 1.09 \text{ s} \tag{7}$$

$$max(f) \neq 0 \tag{8}$$

In the time series signals analysis, the Dynamic Time Warping (DTW) algorithm is often used to calculate the similarity between two time-series signals [35,36]. The data collected from the MEMS sensor is based on a time series, so it is natural to use the DTW algorithm to calculate and measure the similarity of the pulse wave signal. The length of the time series X is m , and the length of the time series Y is n . The similarity distance between the two time series is $dist_{m,n}$. Equation (11) is the iterative formula of the DTW algorithm, in which $dist_{i,j}$ is the DTW distance between a point i on the time series X and a point j on the time series Y , and $d(x_i, y_j)$ is the Euclidean distance between these two points.

$$X = \{x_1, x_2, x_3, \dots, x_m\} \tag{9}$$

$$Y = \{y_1, y_2, y_3, \dots, y_n\} \tag{10}$$

$$dist_{i,j} = \begin{cases} 0, & m = n = 0 \\ \infty, & m = 0|n = 0 \\ d(x_i, y_j) + \min \begin{cases} dist_{i-1,j} \\ dist_{i,j-1} \\ dist_{i-1,j-1} \end{cases} & other \end{cases} \quad (11)$$

$$P_i = \frac{1}{T_0} \int_0^{T_0} |x_i(t)|^2 dt \quad (12)$$

$$y = \frac{P_i}{P_j} * x_j \quad (j = L_2(k); i = P_2(k); k = \{1, 2, \dots\}) \quad (13)$$

$$y = \sum_{i=1}^{12} f(x_i) * g(x_i) * x_i \quad (14)$$

The similarity matrix R was calculated using the DTW algorithm based on the data from the valid waveform. The similarity is sorted from largest to smallest to obtain the ranking vector L_1 of the waveform signal similarity and the ranking vector L_2 of the corresponding subscript. A similar approach was sampled to deal with the average power of the pulse wave over a single acquisition period, a parameter that describes the pulse wave’s energy per unit of time as in Equation (12). Q_1 is the average power ranking vector of M sensors and Q_2 is the ranking vector of the corresponding subscript. L_2 and Q_2 are not identical. The former is related to the array sensor’s overall pulse waveform, while the latter is related to the amplitude of the pulse wave signal. To correct the mismatch between similarity and average power, a linear approach shown in Equation (13) was used. The linear coefficients are related to the similarity ranking vector L_2 and the average power ranking vector Q_2 , where i and j are the values of the k -th element in Q_2 and L_2 , respectively. P_i and P_j are the elements in the ordering vector Q_1 . For a signal with high similarity and low average power, the subscript of the average power sequence is necessarily more incredible than the subscript of the similarity sequence, so $Q_i > Q_j$. The linear adjustment results in an increase in the average power of pulse waves with high similarity, a decrease in the average power of pulse wave signals with low similarity, and no change in the two’s overall average power. The elements in L_1 are traversed sequentially, adjusting the data for the effective waveform linearly until L_2 and Q_2 are identical.

In summary, the entire processing of Algorithm III, as described in Equation (14). $f(x)$ is a discriminant function of pulse wave signal validity, which results in only 0 or 1, $g(x)$ is the linear adjustment factor calculated from the similarity ranking vector and the average power ranking vector, x_i is the pulse wave signal collected by PAWS.

3. Experimental Results

In order to assess the performance of the above methods, multiple repetitions of the test in different test areas are employed under certain standard conditions. The pulse waveform calculated by the pulse wave processing method is theoretically the same as the standard input waveform in two aspects. On the one hand, the method-processed waveform has the same trend as the standard input waveform, which means that the two waveforms are very similar. Consistent with the above, the DTW distance was used to assess the similarity of the two waveforms. On the other hand, the energy of both is identical. Define the gain of the algorithm as the ratio of the energy of the processed signal in a single acquisition cycle to the energy of the standard input signal, as shown in Equation (15), where $x(t)$ is the standard input signal acquired by the ZM-300, $y(t)$ is the processing results of the above method, and T_0 is an acquisition cycle. The smaller the energy difference between the processed signal and the

standard input signal, the closer the system’s gain is to zero. Thus, the degree of energy change after processing by different algorithms can be assessed by gain.

$$Gain = 10 * \log\left(\frac{\int_0^{T_0} |y(t)|^2 dt}{\int_0^{T_0} |x(t)|^2 dt}\right) \tag{15}$$

An SPVG consisting of the ZM-300, periodically squeezing the PAWS’ MEMS sensor array, is used to simulate the pulse wave signal input, as shown in Figure 5a. In Equation (16), the force tested by the sensor in ZM-300 is F_{ZM-300} and the force tested by the sensor array in PAWS is F_{PWAS} . The single-point vibration signal acquired by the former acts as a standard input signal. x_{ZM-300} is the pulse wave signal collected by ZM-300 and x_i is the pulse wave correspondingly collected by the i -th sensor in the PAWS sensor array, as shown in Equations (17) and (18). A and A_i are the amplitude of the waveform, ω is the vibration frequency, t is the time, and φ is the initial phase. The pulse waveform collected by both are almost identical, only differing in amplitude. Figure 5c shows the dynamic pressure waveform collected by the PAWS sensor array.

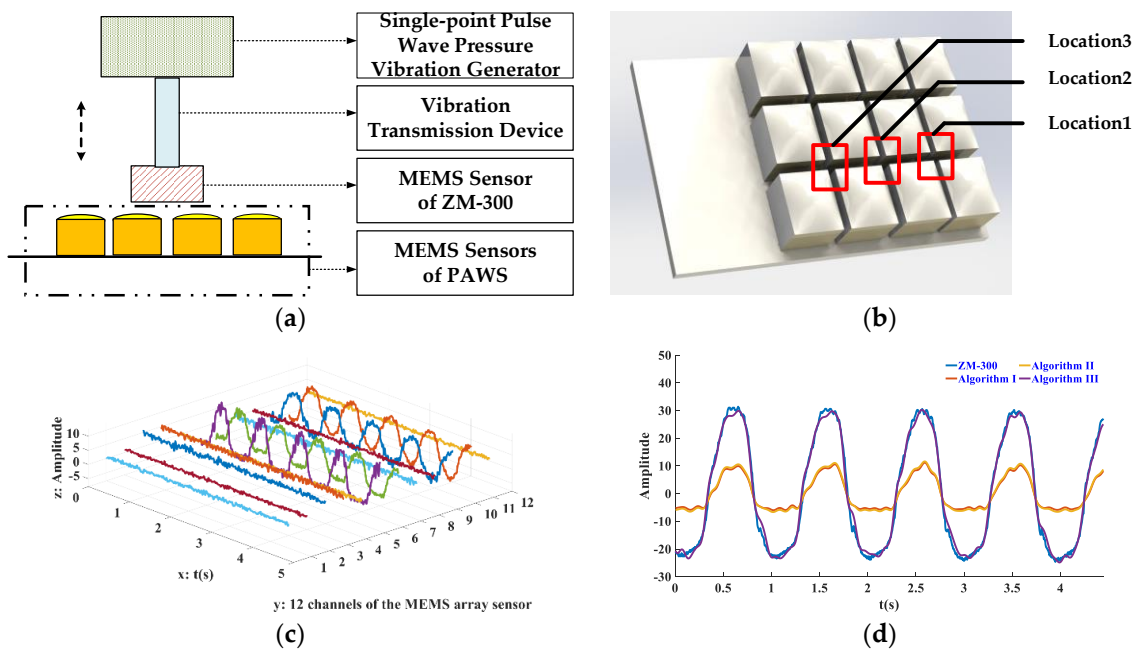


Figure 5. (a) Diagram of SPVG and ZM-300 mutual extrusion; (b) diagram of the test area at three different locations on the PAWS sensor array; (c) pulse waveform graphs collected by twelve sensors in the PAWS sensor array; (d) at location 1, waveforms of the standard input signal and the signal processed by the three algorithms.

As shown in Figure 5b, the SPVG probe’s center is sequentially changed to align at location 1, location 2, and location 3 of PAWS’ sensor array. Six consecutive trials were conducted at each test position to verify the test’s repeatability, just like the method described above. Setting the pressure and vibration frequency of the SPVG to be the same in each experiment ensures the standard input signal’s consistency over multiple experiments. Comparing the algorithm’s processing results and the standard input signal will evaluate the algorithm’s performance.

$$F_{ZM-300} = -F_{PWAS} \tag{16}$$

$$x_{ZM-300} = A \sin(\omega * t + \varphi) \tag{17}$$

$$x_i = A_i \sin(\omega * t + \varphi) \tag{18}$$

In Figure 5d, the blue curves are the standard input signals collected by the ZM-300 at position 1, while the rest are the signal curves processed by the three methods. The waveforms processed by the three algorithms have very similar trends to the standard input signal waveforms, and their phases and frequencies are the same.

The six replicated experiments' standard deviations were 7.2%, 7.0%, and 8.3% at the three test positions, respectively, indicating good repeatability. As shown in Table 1, the DTW distances between the three algorithms' processing results and the standard input signals are quite different. Both Algorithm I and Algorithm II have large DTW distances, while Algorithm III has the smallest DTW distance. Additionally, the gain of different algorithms varies, as shown in Table 2. The gain of Algorithm III is closest to zero, meaning that Algorithm III has the least energy loss in processing results relative to Algorithms I and II.

Table 1. Dynamic Time Warping (DTW) distance of Algorithm I, II, and III processed results with standard input signals.

	Algorithm I	Algorithm II	Algorithm III
Position 1	10.95	10.74	2.38
Position 2	12.48	11.99	2.37
Position 3	10.81	10.81	2.34

Table 2. The gain of Algorithm I, II, and III processed results relative to the standard input signals.

	Algorithm I	Algorithm II	Algorithm III
Position 1	−20.68	−20.17	−1.28
Position 2	−25.24	−23.70	−0.87
Position 3	−20.76	−20.76	−0.80

4. Discussion

This article is intended to provide a novel multi-dimensional composition method based on time series similarity. In order to test the stability and validity of the new algorithm, the methods used by previous workers were summarized in Algorithm I and Algorithm II and analyzed in the same set of collected data [24,27,30]. As mentioned above, we describe and evaluate the algorithms' characteristics in two ways: the degree to which the processing result of the algorithm is close to the standard input signal, including DTW distance and gain; and the magnitude of the change in the processing result of the algorithm in different test areas.

As shown in column 2 of Table 1, the DTW distances between the processing results of Algorithm I and the standard input signal are all greater than 10. Simultaneously, Algorithm II processes very close to Algorithm I, which also has a DTW distance of more than 10, shown in column 3 of Table 1. In contrast, the processing results of Algorithm III are more similar to the standard input signal, with a DTW distance between them of less than 3. The minimum gain value for Algorithm III is −1.28 dB, while the maximum gain value for Algorithm I and II is less than −20 dB, as shown in Table 2. Therefore, Algorithm III outperforms both Algorithm I and II for the property of gain between the algorithm's processing results and the standard input signal.

Comparing the processing results under different test regions reflects the relevance of the algorithm to the test region. The DTW distances between Algorithm I's results and the standard input signals are 10.95, 12.48, and 10.81 at the three test positions, respectively, which change considerably. Simultaneously, Algorithm I has a more remarkable change in gain at the corresponding test location, −20.68 dB, −25.24 dB, and −20.76 dB, respectively, as shown in column 2 of Table 2. Therefore, there is a strong correlation between the processing results of Algorithm I and the test location. Based on the same evaluation method, there is also a correlation between the processing results of Algorithm II and the test location. However, the performance of Algorithm III is more stable under different test regions.

The DTW distances of Algorithm III are 2.38, 2.37, and 2.34 at the three test regions, which is almost indiscriminate. The gain of Algorithm III is also a little changed at all test regions.

Here, we illustrate the variation in sensor test states under different test regions, partly explaining the above algorithms' performance differences. Figure 6 depicts a schematic representation of the sensor contact between SPVG and PAWS at different test positions. At location A, the ZM-300 is in contact with sensor 1, sensor 2, and sensor 3. As in Equation (15), the sum of the dynamic forces tested by the PAWS' sensors is the same as the ZM-300. The dynamic force ratios to total dynamic force tested by sensor 1, sensor 2, and sensor 3 were 10%, 80%, and 10%, respectively. The signal measured by sensor 2 has the highest amplitude value. Therefore, sensor 2 is selected as the representative sensor in Algorithm I, and the pulse wave data collected by sensor 2 is the processing result of Algorithm I. At location B, the ZM-300 is only in contact with sensors 2 and 3, and the latter two share 60% and 40% of the dynamic force. Sensor 2 will continue to be considered as a representative sensor for the entire sensor array in the processing of Algorithm I. However, the dynamic force tested by Sensor 2 has changed, from 60% of the total dynamic force to 80%. Either at position A or position B, Algorithm's representative sensor I acquires only a portion of the entire pulse signal, 80% in the former, and 60% in the latter. Therefore, the energy of Algorithm I's result is less than the standard input signal, which is why the gain value of Algorithm I is less than zero. Furthermore, since the standard input signal's amplitude is the same at both position A and position B, there is a massive difference between the calculation results of Algorithm I at position A and position B.

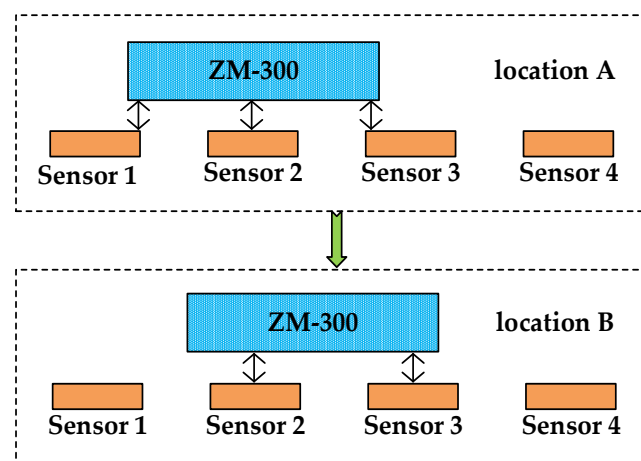


Figure 6. Schematic diagram of sensor contact between SPVG and PAWS at test location A and B.

Since Algorithm II also uses magnitude as an indicator, the reference point is concentrated on sensor 2 at both A and position B positions. Thus, there is some difference between the processing results of Algorithm II and the standard input signal. Subject to the test data of sensor 2, Algorithm II has different calculations at position A and position B. The effect of Algorithm II is very similar to that of Algorithm I.

The processing of Algorithm III takes advantage of the spatial characteristics of the array sensors to extract as much commonality and retain all valid data information as possible. First, at position A, algorithm III considers the acquisition results of sensor 1, sensor 2, and sensor 3. Algorithm III was linearly adjusted to obtain a waveform that was as similar as possible to the standard input signal. Finally, linear synthesis ensures that there is not much energy lost during the processing of Algorithm III. As a result, Algorithm III's processing is much closer to the standard input signal, both in waveform shape and energy. The same standard input signal at different positions ensures that Algorithm III's results are also nearly similar. Compared to Algorithm I and Algorithm II, Algorithm III has good robustness at position A and position B.

5. Conclusions

A one-dimensional pulse wave signal extracted from a spatial multi-dimensional signal collected by a pressure-based sensor array is beneficial for disease diagnosis. However, the existing methods have some shortcomings, and the processing results in the multiple acquisition process are not the same. Therefore, this paper proposes a novel multi-dimensional composition method based on time series similarity. The new method includes filtering, effective waveform screening, linear adjustment, and linear synthesis to obtain stable results under different test regions. Design a simulated pulse wave acquisition experiment composed of PAWS and SPVG, which is repeated tests in different positions to verify three algorithms' performance. The experimental results show that the proposed method can virtually reproduce the standard input waveform well and has the right consistency and stability.

In summary, the new method is a suitable replacement for the previous method, thus providing physicians with a better basis for pulse wave diagnosis. We will continue to improve the algorithm's reliability by adopting a more refined modeling approach in future work. We also believed that this work would help in the promotion of pulse-wave-assisted diagnosis.

6. Patents

The works presented in this paper are subject to pending China and international patents filed by the Institute of Microelectronics of Chinese Academy of Sciences (IMECAS) in China (201910570914.4, 201910570913.X, PCT/CN2019/093154, and PCT/CN2019/093156).

Author Contributions: Conceptualization, H.Z. (Hongjie Zou), and Y.Z.; data curation, H.Z. (Hongjie Zou); formal analysis, H.Z. (Hongjie Zou), J.Z., S.Z., and Y.Z.; funding acquisition, H.Z. (Haiying Zhang); investigation, H.Z. (Hongjie Zou); methodology, H.Z. (Hongjie Zou), and Y.Z.; project administration, Y.Z., and H.Z. (Haiying Zhang); resources, Y.Z., J.Z., H.Z. (Haiying Zhang); algorithm, H.Z. (Hongjie Zou); software, H.Z. (Hongjie Zou), X.G., and C.C.; supervision, H.Z. (Haiying Zhang); validation, H.Z. (Hongjie Zou), J.Z., C.C., X.G., S.Z., and Y.Z.; visualization, H.Z. (Hongjie Zou), and C.C.; writing—original draft, H.Z. (Hongjie Zou); writing—review and editing, H.Z. (Hongjie Zou), Y.Z., and H.Z. (Haiying Zhang). All authors have read and agreed to the published version of the manuscript.

Funding: This research was funded by the National Science and Technology Major Project (No. 2018ZX01031201), the National Key Research and Development Program (No. 2018YFC2001100), and the Key Program of the Chinese Academy of Sciences (No. KFZD-SW-218).

Conflicts of Interest: The authors declare no conflict of interest.

References

- Chirakanphaisarn, N.; Thongkanluang, T.; Chiwpreechar, Y. Heart rate measurement and electrical pulse signal analysis for subjects span of 20–80 years. In Proceedings of the 2016 6th International Conference on Digital Information Processing and Communications, Beirut, Lebanon, 21–23 April 2016; pp. 112–120.
- Cruickshank, K.; Riste, L.; Anderson, S.G.; Wright, J.S.; Dunn, G.; Gosling, R.G. Aortic Pulse-Wave Velocity and Its Relationship to Mortality in Diabetes and Glucose Intolerance: An Integrated Index of Vascular Function? *Circulation* **2002**, *106*, 2085–2090. [[CrossRef](#)] [[PubMed](#)]
- Koizumi, M.; Shimizu, H.; Shimomura, K.; Oh-I, S.; Tomita, Y.; Kudo, T.; Iizuka, K.-I.; Mori, M. Relationship between hyperinsulinemia and pulse wave velocity in moderately hyperglycemic patients. *Diabetes Res. Clin. Pr.* **2003**, *62*, 17–21. [[CrossRef](#)]
- Huang, C.-J.; Lin, H.-J.; Liao, W.-L.; Ceurvels, W.; Su, S.-Y. Diagnosis of traditional Chinese medicine constitution by integrating indices of tongue, acoustic sound, and pulse. *Eur. J. Integr. Med.* **2019**, *27*, 114–120. [[CrossRef](#)]
- Jiang, Z.; Guo, C.; Zang, J.; Lu, G.; Zhang, D. Features fusion of multichannel wrist pulse signal based on KL-MGDCCA and decision level combination. *Biomed. Signal Process. Control* **2020**, *57*, 101751. [[CrossRef](#)]
- De Moura, N.G.R.; Ferreira, A.D.S. Pulse Waveform Analysis of Chinese Pulse Images and Its Association with Disability in Hypertension. *J. Acupunct. Meridian Stud.* **2016**, *9*, 93–98. [[CrossRef](#)]
- Jin, C.; Xia, C.; Zhang, S.; Wang, L.; Wang, Y.; Yan, H. A Wearable Combined Wrist Pulse Measurement System Using Airbags for Pressurization. *Sensors* **2019**, *19*, 386. [[CrossRef](#)]

8. Chung, Y.-F.; Hu, C.-S.; Yeh, C.-C.; Luo, C.-H. How to standardize the pulse-taking method of traditional Chinese medicine pulse diagnosis. *Comput. Biol. Med.* **2013**, *43*, 342–349. [[CrossRef](#)]
9. Murphy, J.C.; Morrison, K.; McLaughlin, J.; Manoharan, G.; Adgey, A.J. An Innovative Piezoelectric-Based Method for Measuring Pulse Wave Velocity in Patients With Hypertension. *J. Clin. Hypertens* **2011**, *13*, 497–505. [[CrossRef](#)]
10. Clemente, F.; Arpaia, P.; Cimmino, P. A piezo-film-based measurement system for global haemodynamic assessment. *Physiol. Meas.* **2010**, *31*, 697–714. [[CrossRef](#)]
11. McLaughlin, J.; McNeill, M.; Braun, B.; McCormack, P.D. Piezoelectric sensor determination of arterial pulse wave velocity. *Physiol. Meas.* **2003**, *24*, 693–702. [[CrossRef](#)]
12. Wang, P.; Zuo, W.; Zhang, D. A Compound Pressure Signal Acquisition System for Multichannel Wrist Pulse Signal Analysis. *IEEE Trans. Instrum. Meas.* **2014**, *63*, 1556–1565. [[CrossRef](#)]
13. Chen, Y.; Lu, B.; Chen, Y.; Feng, X. Biocompatible and Ultra-Flexible Inorganic Strain Sensors Attached to Skin for Long-Term Vital Signs Monitoring. *IEEE Electron Device Lett.* **2016**, *37*, 496–499. [[CrossRef](#)]
14. Wang, Z.; Wang, S.; Zeng, J.; Ren, X.; Chee, A.J.Y.; Yiu, B.Y.S.; Chung, W.C.; Yang, Y.; Yu, A.C.H.; Roberts, R.C.; et al. High Sensitivity, Wearable, Piezoresistive Pressure Sensors Based on Irregular Microhump Structures and Its Applications in Body Motion Sensing. *Small* **2016**, *12*, 3827–3836. [[CrossRef](#)] [[PubMed](#)]
15. Loukogeorgakis, S.; Dawson, R.; Phillips, N.; Martyn, C.N.; Greenwald, S.E. Validation of a device to measure arterial pulse wave velocity by a photoplethysmographic method. *Physiol. Meas.* **2002**, *23*, 581–596. [[CrossRef](#)]
16. Lovinsky, L.S. Urgent Problems of Metrological Assurance of Optical Pulse Oximetry. *IEEE Trans. Instrum. Meas.* **2006**, *55*, 869–875. [[CrossRef](#)]
17. Wang, D.; Zhang, D.; Lu, G. A Novel Multichannel Wrist Pulse System with Different Sensor Arrays. *IEEE Trans. Instrum. Meas.* **2015**, *64*, 2020–2034. [[CrossRef](#)]
18. Couade, M.; Pernot, M.; Prada, C.; Messas, E.; Emmerich, J.; Bruneval, P.; Criton, A.; Fink, M.; Tanter, M. Quantitative Assessment of Arterial Wall Biomechanical Properties Using Shear Wave Imaging. *Ultrasound Med. Biol.* **2010**, *36*, 1662–1676. [[CrossRef](#)]
19. Huang, C.; Ren, T.-L.; Luo, J. Effects of parameters on the accuracy and precision of ultrasound-based local pulse wave velocity measurement: A simulation study. *IEEE Trans. Ultrason. Ferroelectr. Freq. Control.* **2014**, *61*, 2001–2018. [[CrossRef](#)]
20. Xue, Y.; Su, Y.; Zhang, C.; Xu, X.; Gao, Z.; Wu, S.; Zhang, Q.; Wu, X. Full-field wrist pulse signal acquisition and analysis by 3D Digital Image Correlation. *Opt. Lasers Eng.* **2017**, *98*, 76–82. [[CrossRef](#)]
21. Liu, S.; Zhang, S.; Zhang, Y.; Geng, X.; Zhang, J.; Zhang, H. A novel flexible pressure sensor array for depth information of radial artery. *Sensors Actuators A Phys.* **2018**, *272*, 92–101. [[CrossRef](#)]
22. Luo, C.-H.; Chung, Y.-F.; Hu, C.-S.; Yeh, C.-C.; Si, X.-C.; Feng, D.-H.; Lee, Y.-C.; Huang, S.-I.; Yeh, S.-M.; Liang, C.-H. Possibility of quantifying TCM finger-reading sensations: I. Bi-Sensing Pulse Diagnosis Instrument. *Eur. J. Integr. Med.* **2012**, *4*, e255–e262. [[CrossRef](#)]
23. Luo, C.-H.; Su, C.-J.; Huang, T.-Y.; Chung, C.-Y. Non-invasive holistic health measurements using pulse diagnosis: I. Validation by three-dimensional pulse mapping. *Eur. J. Integr. Med.* **2016**, *8*, 921–925. [[CrossRef](#)]
24. Hu, C.-S.; Chung, Y.-F.; Yeh, C.-C.; Luo, C.-H. Temporal and Spatial Properties of Arterial Pulsation Measurement Using Pressure Sensor Array. *Evid. Based Complement. Altern. Med.* **2011**, *2012*, 1–9. [[CrossRef](#)]
25. Fei, Z. *Contemporary Sphygmology in Traditional Chinese Medicine*; People's Medical Publishing House: Beijing, China, 2003; pp. 205–227.
26. Chou, H.-C.; Lin, K.-J.; Fang, Y.-X.; Liou, J.-F. Development a polymer-based electronic pulse diagnosis instrument for measuring and analyzing pulse wave velocity. *Technol. Health Care* **2015**, *24*, S83–S95. [[CrossRef](#)] [[PubMed](#)]
27. Chen, C.; Li, Z.; Zhang, Y.; Zhang, S.; Hou, J.; Zhang, H. A 3D Wrist Pulse Signal Acquisition System for Width Information of Pulse Wave. *Sensors* **2019**, *20*, 11. [[CrossRef](#)] [[PubMed](#)]
28. Chen, J.-X.; Liu, F. Research on characteristics of pulse delineation in TCM & omnidirectional pulse detecting by electro-pulsograph. In Proceedings of the 2008 IEEE International Symposium on IT in Medicine and Education, Xiamen, China, 12–14 December 2008; pp. 536–538.
29. Cui, J.; Tu, L.-P.; Zhang, J.-F.; Zhang, S.-L.; Zhang, Z.-F.; Xu, J.-T. Analysis of Pulse Signals Based on Array Pulse Volume. *Chin. J. Integr. Med.* **2018**, *25*, 103–107. [[CrossRef](#)]

30. Peng, B.; Luo, C.-H.; Chan, W.Y.; Shieh, M.-D.; Su, C.-J.; Tai, C.-C. Development and Testing of a Prototype for 3D Radial Pulse Image Measurement and Compatible With 1D Pulse Wave Analysis. *IEEE Access* **2019**, *7*, 182846–182859. [[CrossRef](#)]
31. Cong-Ying, L. Study on the pressure methods of pulse detecting instrument. In Proceedings of the 2013 IEEE International Conference on Bioinformatics and Biomedicine, Shanghai, China, 18–21 December 2013; pp. 38–42.
32. Jia, D.; Li, N.; Liu, S.; Li, S. Decision level fusion for pulse signal classification using multiple features. In Proceedings of the 2010 3rd International Conference on Biomedical Engineering and Informatics, Yantai, China, 16–18 October 2010; pp. 843–847.
33. Keys, R. Cubic convolution interpolation for digital image processing. *IEEE Trans. Acoust. Speech Signal Process.* **1981**, *29*, 1153–1160. [[CrossRef](#)]
34. Jiang, Z.; Zhang, D.; Lu, G. A Robust Wrist Pulse Acquisition System Based on Multisensor Collaboration and Signal Quality Assessment. *IEEE Trans. Instrum. Meas.* **2019**, *68*, 4807–4816. [[CrossRef](#)]
35. Müller, M. *Information Retrieval for Music and Motion*; Springer: Berlin/Heidelberg, Germany, 2007; pp. 69–84. [[CrossRef](#)]
36. Berndt, D.J.; Clifford, J. Using dynamic time warping to find patterns in time series. In Proceedings of the KDD Workshop, Seattle, WA, USA, 31 July–1 August 1994; pp. 359–370.

Publisher’s Note: MDPI stays neutral with regard to jurisdictional claims in published maps and institutional affiliations.



© 2020 by the authors. Licensee MDPI, Basel, Switzerland. This article is an open access article distributed under the terms and conditions of the Creative Commons Attribution (CC BY) license (<http://creativecommons.org/licenses/by/4.0/>).